CALIBRATION AND IMAGE RECONSTRUCTION FOR THE HURRICANE IMAGING RADIOMETER (HIRAD)

Christopher Ruf[1], J. Brent Roberts[2], Sayak Biswas[2], Mark James[2] and Timothy Miller[2]

[1]University of Michigan, Ann Arbor, MI USA

[2] NASA, Marshall Space Flight Center, Huntsville, AL USA

ABSTRACT

The Hurricane Imaging Radiometer (HIRAD) is a new airborne passive microwave synthetic aperture radiometer designed to provide wide swath images of ocean surface wind speed under heavy precipitation and, in particular, in tropical cyclones. It operates at 4, 5, 6 and 6.6 GHz and uses interferometric signal processing to synthesize a pushbroom imager in software from a low profile planar antenna with no mechanical scanning. The retrieval algorithm (and the HIRAD instrument itself) is a direct descendant of the nadir-only Stepped Frequency Microwave Radiometer that is used operationally by the NOAA Hurricane Research Division to monitor Tropical Cyclones [1,2]. HIRAD participated in NASA's Genesis and Rapid Intensification Processes (GRIP) mission during Fall 2010 as its first science field campaign. HIRAD produced images of upwelling brightness temperature over a ~70 km swath width with ~3 km spatial resolution. The calibration and image reconstruction algorithms that were used to verify HIRAD functional performance during and immediately after GRIP were only preliminary and used a number of simplifying assumptions and approximations about the instrument design and performance. The development and performance of a more detailed and complete set of algorithms are reported here.

Index Terms—*Tropical Cyclone, Imager, Aperture Synthesis Microwave Radiometer*

1. HIRAD INSTRUMENT OVERVIEW

The HIRAD planar antenna is composed of linear arrays of stacked multi-resonant radiators, operating at 4, 5, 6, and 6.6 GHz [3]. Each linear array, viewed as an individual fan beam antenna element, is placed in an optimum thinned array configuration to produce the interferometer baselines needed for aperture synthesis. Individual receivers after each fan beam element contain internal hot and cold calibration loads. A single correlated noise diode is also distributed to all receivers to calibrate the interferometric correlation measurements [4]. HIRAD's major components consist of the integrated stacked patch antenna array, analog receivers with integrated calibration sources, real time digital signal processing for frequency sub-banding, RFI mitigation and interferometric cross-correlation, command and data handling, and the Power Distribution Unit, which includes thermal control for the instrument.

2. CALIBRATION ALGORITHM

The basic signal flow through the radiometer for self-correlation measurements made by individual HIRAD receivers is shown in Fig. 1. In the figure, T_A is the incident brightness temperature weighted by the antenna pattern of an individual HIRAD antenna, L is the net transmissivity of the lossy radome and antenna, T_{iso} is the physical temperature of the radome and antenna, T_A' is the effective antenna temperature after propagation through the radome and antenna (including self emission by the lossy elements), T_W and T_C are the brightness temperatures of the internal warm and cold calibration loads, T_{ND} is the increase in brightness temperature due to the noise diode, G is the receiver gain in units of Kelvins/counts, and C_X is the raw 2nd moment counts when the system is in state X. Possible system states include: X = A (viewing the antenna), W (warm load), C (cold load), W+ND (warm load with noise diode on), and C+ND (cold load with noise diode on).

The T_A calibration algorithm is given be

$$T_A = [T_A' - (1 - L)T_{iso}]L^{-1} \quad (1)$$

where

$$G = (T_W - T_C)/(C_W - C_C) \quad (2)$$

and

$$T_A' = T_W - dT_{RX} - (C_W - C_A)G \quad (3)$$

Equations (1)-(3) constitute the zero'th Visibility (V_0) calibration algorithm. V_0 corresponds to the average brightness temperature over the complete cross-track swath of the imager.

The basic signal flow through the radiometer for cross-correlation measurements made by pairs of HIRAD receivers is shown in Fig. 2.

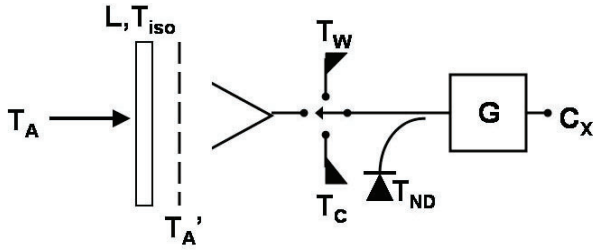

Figure 1. Signal flow diagram for HIRAD self correlation measurements.

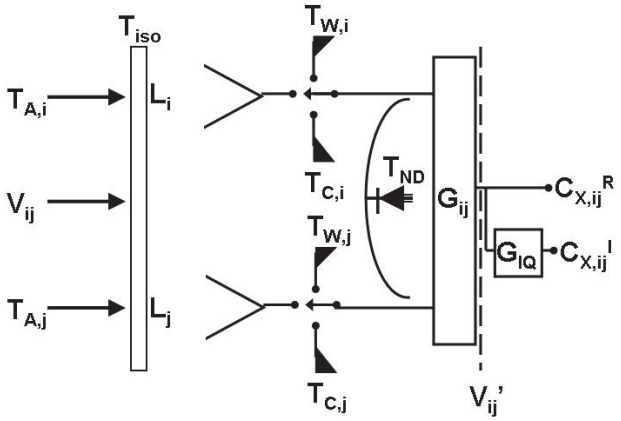

Figure 2. Signal flow diagram for HIRAD cross correlation measurements.

In Fig. 2, incident T_A signals enter the i^{th} and j^{th} channels of HIRAD. The antenna transmissivity, L, and the warm and cold reference brightness temperatures, T_W and T_C, are in general different for each channel. A single noise diode is common to all ten HIRAD channels to provide a correlated signal, but its additive brightness temperature is in general different for each channel. G_{ij} is the cross-correlation gain for the i^{th} and j^{th} channels. $C_{X,ijR}$ and $C_{X,ijI}$ represent the real and imaginary components of the raw cross-correlation counts when the system is in state X, and G_{IQ} represents the gain imbalance between the two complex components.

The Visibility calibration algorithm is given by

$$V_{ijR}' = (C_{A,ijR} - C_{0,ijR})G_{ij}L_{ij}^{-1} \quad (4a)$$

and

$$V_{ijI}' = (C_{A,ijI} - C_{0,ijI})G_{IQ}G_{ij}L_{ij}^{-1} \quad (4b)$$

where the cross-correlation gain is found as the geometric mean of the appropriate pair of self-correlation gains. If G_i is the self-correlation gain for receiver i, given by (5), then

$$G_{ij} = (G_iG_j)^{1/2} \quad (5)$$

Equations (4)-(5) constitute the non-zero Visibility calibration algorithm.

3. EXAMPLE OF V_0 CALIBRATION PERFORMANCE

Time series plots of the calibrated zero'th visibility, V_0, measurements made by HIRAD at 5 GHz are shown in Fig. 3 for two airborne flights. The total passband is divided digitally into 16 subbands to aid in the detection and mitigation of radio frequency interference, and the individual V_0 values for each subband are shown. The NEDT noise level is high for the individual subband data and is reduced when they are averaged together. The left plot shows V_0 during a test flight made on 11 March 2010 during engineering commissioning. The brightness at the beginning of the flight is high while the aircraft is over land. V_0 drops rapidly at the coastal crossing, then remains low and steady during the flight segment over calm, open water in the Gulf of Mexico. The final portion of the left hand plot shows the rise in V_0 as the plan begins to cross back over land. The right hand plot shows V_0 during the Hurricane Karl overpass on 16 September 2010. Very high V_0 levels at the beginning and end correspond to over-land flight segments. Rapidly varying V_0 values in the middle correspond to overpasses of Karl, together with aircraft bank maneuvers between overpass flight legs.

4. EXAMPLE OF T_B IMAGING PERFORMANCE

The complete set of visibility samples is calibrated using equations (1)-(5). Brightness temperature (T_B) images are

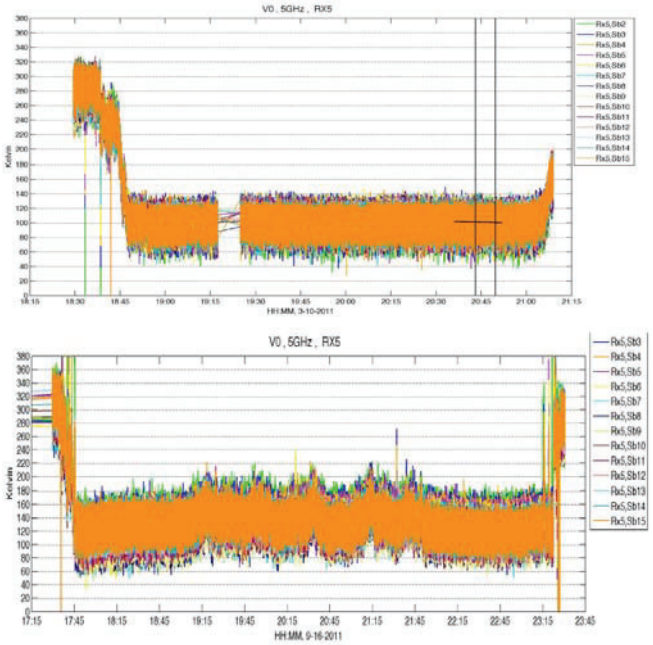

Figure 3. Time series plots of the average brightness temperature across the HIRAD swath at 5 GHz for two aircraft flights. (top) 11 March 2010 test flight over clear, calm ocean. (bottom) GRIP overpass of Hurricane Karl on 16 September 2010.

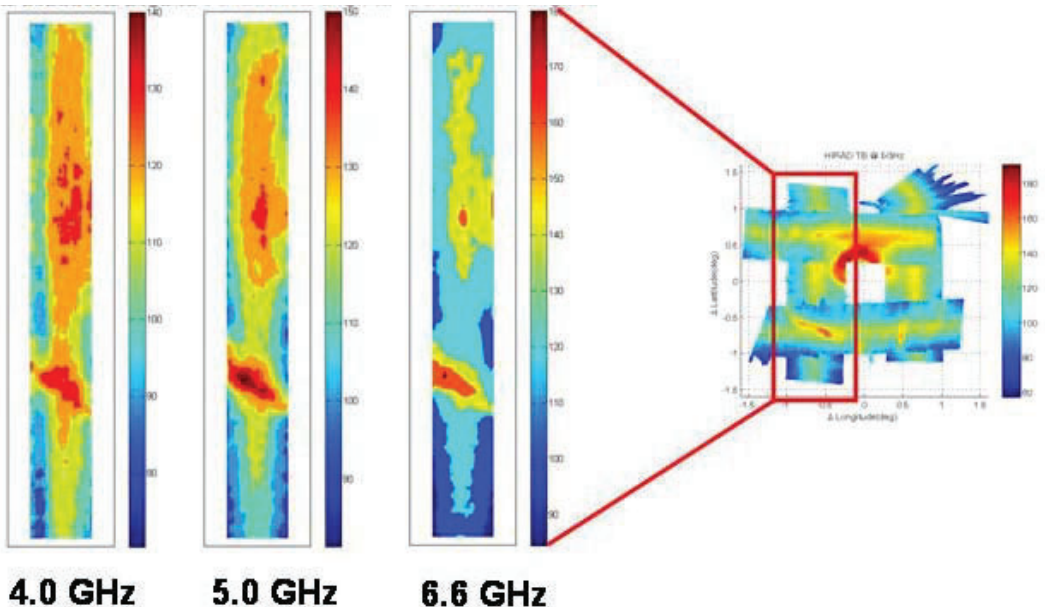

Figure 4. HIRAD T_B images during overflight of Hurricane Earl on 1 September 2010. 5.0 GHz T_B for four successive passes around the eye are shown at right. Simultaneous observations at 3 frequencies during the south-to-north pass are shown at left.

generated from the visibilities by a least squares pseudo-inverse of the individual spatial interference patterns that are formed by the correlation between antenna elements. The image reconstruction algorithm uses the "G-matrix" approach to perform the pseudo-inverse [5].

An example of HIRAD's T_B imaging performance is provided by a Hurricane Earl overflight performed on 1 September 2010 as part of the GRIP campaign. T_B images at 4, 5 and 6.6 GHz are shown in Fig. 4 during a south-to-north pass over the western edge of the eyewall. Several features in the images are noteworthy. The component of T_B that originates from surface emission decreases away from the center of the swath at all frequencies due to the increasing incidence angle. Localized areas of increased T_B which are comparable at all frequencies correspond to higher surface wind speeds, which raise the surface emissivity approximately the same at all frequencies. Localized areas of increased T_B which increase more with increasing frequency correspond to the presence of precipitation, which has an emission spectrum that scales roughly as the square of frequency. In the three south-to-north T_B strip chart images in Fig. 4, for example, the high precipitation levels present in the western eyewall are indicated by the successively higher T_B levels with increasing frequency in the northern portion of the image.

7. REFERENCES

[1] Jones, W. L., P. G. Black, V. E. Delnore, and C. T. Swift, Airborne Microwave Remote Sensing Measurements of Hurricane Allen, *Science*, 214, 274-280, 1981.

[2] Uhlhorn, E. W., P. G. Black, J. L. Franklin, M. Goodberlet, J. Carswell and A. S. Goldstein, "Hurricane surface wind measurements from an operational stepped-frequency microwave radiometer," *Mon. Wea. Rev.*, **135**(9): 3070-3085, 2007.

[3] Bailey, M.C., R. Amarin, J. Johnson, P. Nelson, M. James, D. Simmons, C. Ruf, L. Jones and X. Gong, "Multi-Frequency Synthetic Thinned Array Antenna for the Hurricane Imaging Radiometer," *Trans. Antennas Propagat.*, 58(8), doi:10.1109/TAP.2010.2050453, 2010.

[4] Ruf, C., R. Amarin, M.C. Bailey, B. Lim, R. Hood, M. James, J. Johnson, L. Jones, V. Rohwedder and K. Stephens, "The hurricane imaging radiometer – An octave bandwidth synthetic thinned array radiometer," Proc. IGARSS 2007, Barcelona, 23-27 July 2007.

[5] Tanner, A. B., and C. T. Swift, "Calibration of a Synthetic Aperture Radiometer," *IEEE Trans. Geosci. Remote Sens.*, 31(1) 257-267, 1993.